
Chemistry
Europe
Excellence in Chemistry Research Worldwide
Front Cover:
Photo by Rodion Kutsalev on Unsplash
journal.chemistry-europe.org
WILEY-VCH

ChemistrySelect

Research Article
doi.org/10.1002/slct.202204798

Chemistry Europe
European Chemical Societies Publishing

www.chemistryselect.org

Controlled Delivery of Amoxicillin and Rifampicin by Three-Dimensional Polyvinyl alcohol/Bismuth Ferrite Scaffolds

Sule Ilgar,[a, b] Songul Ulag,*[a, c, f] Ali Sahin,[d, e] Oguzhan Gunduz,[a, c, f] and
Cem Bulent Ustundag[a, b, f]

Skin is a protective barrier that can protect against environmental influences and renew itself. However, in some cases, this regenerative property is lost, and this causes delays in wound healing. Wound healing is a complex and long-lasting phase. Any bacterial infection during the wound healing process delays wound healing. The therapeutic efficacy can be increased by using nanocarrier drug delivery systems to the target tissue with modern wound dressings. Controlled nano drug delivery systems increase the therapeutic efficacy in the treatment of diseases and provide a faster recovery process. In this study, amoxicillin (AMX) and rifampicin (RIF) were loaded into the bismuth ferrite (BFO) particles which were synthesized with the co-precipitation method. Then, these drug-loaded BFO particles (0.075%) were added separately to 13% polyvinyl alcohol (PVA) solution and the solutions were printed three-dimensionally to obtain three dimensional scaffolds. With these designed scaffolds, it is aimed to reduce the risk of inflammation in wound tissues and increase therapeutic efficacy with controlled release. The SEM images proved that homogeneous pore distributions could be achieved with these combinations. The tensile test results showed that drug-loaded BFO addition increased the mechanical strength of the 13% PVA scaffold. The biocompatibility test results demonstrated that the highest viability values of the human adipose tissue-derived mesenchymal stem cells were obtained for AMX-added 13% PVA scaffolds.

Introduction

The increase in the number of people worldwide with chronic wounds that are difficult to heal (4 million patients per year in Europe alone) places a significant burden on society and health systems as it requires long hospital stays and costly treatments. In addition, patients with decreased wound healing have to live with a low quality of life due to the difficulty of controlling the pain caused by chronic wounds.[1] Skin is a protective barrier against environmental hazards.[2] It has regenerative properties, and wounds or cuts on the skin can be healed through a highly regulated cascade of physiological events in the human body. However, in some cases, this regenerative property is impaired, and wounds do not heal in time, putting patients at significant health risk.[3] Additionally, pain is known to cause delays in wound healing. Therefore, providing appropriate therapeutic solutions for less painful wound healing is receiving more attention in developing future wound care solutions.[4] The traditional dressings are in the form of gauze, plasters, and bandages, while modern dressings are in the form of films, foams, hydrogels, and hydrocolloids. They absorb and dry out wound exudates when applied over the wound. When they are taken out, they remove some of the tissue around the wound, which increases the infection. A low oxygen permeability, a lack of biomimicry, and difficulties with adequate drug loading are some additional negative effects of conventional dressings. In addition, modern dressings can increase epidermal migration, promote angiogenesis, provide gas exchange, and protect against pathogens.[5,6] Also, better wound healing can be achieved by using nanocarrier drug delivery systems in these modern wound dressings.[7] Controlled delivery can provide an excellent means of delivering drugs to wound sites consistently and adequately without the need for frequent dressing changes. The dressing that will deliver an active substance to the wound area in a controlled manner for a long period causes an increase in its therapeutic effectiveness.[8] Drug delivery systems are particularly important because of the inability to deliver adequate doses of the drug to tissues when the drug is administered systemically. In addition, the side effects of some drugs, the low half-life of biological factors, and the dynamism of the wound environment require drug delivery systems to deliver drug molecules to the target tissue at the appropriate dose.[9] Nanoparticles have several advantages in drug delivery systems. Due to their internal volume or large surface area, large amounts of drugs can be loaded into the nanoparticle.[10] Drug-loaded nanoparticles can penetrate host cells via endocytosis and subsequently release drug payloads to treat microbe-caused intra-

---

[a] S. Ilgar, Dr. S. Ulag, Prof. O. Gunduz, Prof. C. B. Ustundag
Center for Nanotechnology & Biomaterials Application and Research (NBUAM), Marmara University, Turkey
E-mail: songul.ulag@marmara.edu.tr
[b] S. Ilgar, Prof. C. B. Ustundag
Department of Bioengineering, Faculty of Chemistry and Metallurgy, Yildiz Technical University, Turkey
[c] Dr. S. Ulag, Prof. O. Gunduz
Department of Metallurgical and Materials Engineering, Faculty of Technology, Marmara University, Turkey
[d] Dr. A. Sahin
Department of Biochemistry, Faculty of Medicine, Marmara University, Turkey
[e] Dr. A. Sahin
Genetic and Metabolic Diseases Research and Investigation Center (GEMHAM), Marmara University, Turkey
[f] Dr. S. Ulag, Prof. O. Gunduz, Prof. C. B. Ustundag
Health Biotechnology Joint Research and Application Center of Excellence, Yildiz Technical University, Turkey

cellular infections.[11] It can be used to treat different diseases by adding more than one drug molecule simultaneously. Due to its nano-sized structures, it can stay in the body for a long time, which can increase the therapeutic effectiveness of the drug. Due to these benefits, nanoparticles have emerged as potential new medication carriers in therapeutic settings.[12] Recent research has shown that materials with both magnetic and electrical properties are of interest to researchers looking to develop new materials or structures due to their controlled abilities.[13] Multiferroics are materials with electrical, magnetic, and structural order properties that simultaneously produce ferroelectric, ferromagnetism, and ferroelasticity effects in the same material.[14] Bismuth ferrite (BFO) is a multiferroic material at room temperature with magnetically arranged and high thermal stability ferroelectric states.[15] It is a semiconductor with a narrow bandgap in the visible light range of 2.1 to 2.8 eV. Due to this property, it can also be utilised as a photocatalyst.[16,17] Polyvinyl alcohol (PVA), a hydrophilic, biodegradable, and biocompatible semicrystalline synthetic polymer, is widely used in various biomedical applications.[18–20] It is one of the polymers that are most frequently used in the biomedical industry because of its mechanical qualities, high film-forming capacity, non-toxicity, water solubility, non-carcinogenicity, hydrophilicity, good compatibility with human tissues and fluids, and biodegradability.[21] In addition, the highly hydrophilic nature of PVA increases its solubility when conjugated with carriers and drugs.[22] In this study, Amoxicillin (AMX) and Rifampicin (RIF) loaded BFO particles were added into the 13 % PVA solution, and 13 % PVA/BFO, 13 % PVA/BFO_RIF, and 13 % PVA/BFO_AMX scaffolds were fabricated using a 3D printing process to observe the release behaviours of the drugs from the scaffolds. 3D printing is about overlapping layers of material to create 3D models. Thus better controlling pore sizes, pore morphology, and porosity of the matrix compared to other fabrication methods.[23] The hydrophilic drug amoxicillin has a high capacity for hydration as well as an antimicrobial effect.[24] Rifampicin is a hydrophobic antibiotic with bactericidal action.[25,26] The release behaviours of these drugs from the scaffolds were investigated with in-body fluids at different time intervals.

Experimental Section

Materials

Iron (III) nitrate nonahydrate ($Fe(NO_3)_3*9H_2O$, MW = 403.95 g/mol), Bismuth (III) nitrate ($Bi_5O(OH)_9(NO_3)_4$, MW = 1.461,99 g/mol) and Nitric acid (65 %) were bought-in Merck KGaA, Germany. Ammonia Solution (25 %, MW = 35.05 g/mol) was purchased from ISOLAB (Wertheim, Germany). Polyvinyl alcohol (PVA, MW = 89,000–98,000, 99 + % hydrolysed) was bought in Sigma Aldrich (USA). The distilled water was provided by a water distiller (MP MINIPURE). The amoxicillin (MW = 365.4 g/mol) and rifampicin (MW 822.94 g/mol) were bought from Sigma Aldrich (USA).

Synthesis of AMX and RIF Loaded BFO Particles with Co-precipitation Method

Bismuth ferrite particles were synthesised by the co-precipitation method. This method allows water-soluble particles to be directly obtained with a high yield in a simple process. Firstly, 1.86 g of $Bi(NO_3)_3$ $5H_2O$ was mixed in 10 mL of nitric acid in a magnetic stirrer at 300 rpm for 30 minutes. Then 2.58 g of iron nitride ($Fe(NO_3)_3.9H_2O$) was mixed in 10 mL of distilled water at 300 rpm for 15 minutes. After two solutions were completely dissolved, the two solutions were mixed in the same beaker, and 20 mg of AMX was added to it and mixed at 300 rpm for 30 minutes to obtain a homogeneous mixture. The same procedure also was applied for 20 mg of RIF. Then the solution was stirred on a magnetic stirrer at 300 rpm for 60 minutes. Then, ammonia solution was added to BFO_AMX and BFO_RIF solutions separately until the pH value reached 10.04 at room temperature. The formed precipitate was filtered through filter paper and washed several times with distilled water. Then, the resulting powders were dried in an oven at 100 °C for 24 hours, and AMX and RIF-loaded BFO particles were obtained.

Preparation of the 13 % PVA, 13 % PVA/BFO_AMX, and 13 % PVA/BFO_RIF Solutions

1.3 g PVA was dissolved in 10 mL of distilled water, and the prepared 13 % PVA solution was put in the magnetic stirrer at 90 °C, 300 rpm. The 7.5 mg of BFO/AMX and BFO/RIF particles were added into the 13 % PVA solution separately and mixed in the magnetic stirrer at 300 rpm, room temperature. Then, the prepared 13 % PVA/BFO_AMX and 13 % PVA/BFO_RIF solutions were sonicated for 10 minutes to obtain more homogeneous solutions.

Fabrication of the Scaffolds

The Solidworks program was used to design the dimensions of the scaffold (20x20x1 mm^3). The prepared solutions were loaded into a 10 mL syringe attached to a needle with a 0.2 mm diameter value. In the 3D printing process, scaffolds with 8-layer were produced at a 10 mm/s printing speed, 1 mL/h flow rate, and 96 % infill percentage. After the fabrication, 5 mL of Glutaraldehyde (GA) was put on the desiccator with scaffolds, and they were put together in the oven at 60 °C for 3 hours. Then, the scaffolds were crosslinked with GA vapour. The preparation of the solutions and fabrication of the scaffolds were summarized in Figure 1.

Physical Properties of the Prepared Solutions

The density, surface tension, and viscosity measurements of all the solutions were performed at room temperature. All equipment was calibrated before the tests, and each test was repeated three times. The density values of the solutions were determined using a standard density bottle (10 mL, DIN ISO 3507-Gay-Lussac Boru Cam Inc., Republic of Turkey). The surface tension values of the prepared solutions were measured using a force tensiometer (Sigma 703D, Caution, Germany). The viscosity values of all prepared solutions were determined using a digital viscometer (DV-E, Brookfield AMETEK, USA).

Fourier Transform Infrared Spectroscopy (FT-IR)

The molecular structure of the scaffolds and the presence of chemical groups were analysed using Fourier transform infrared

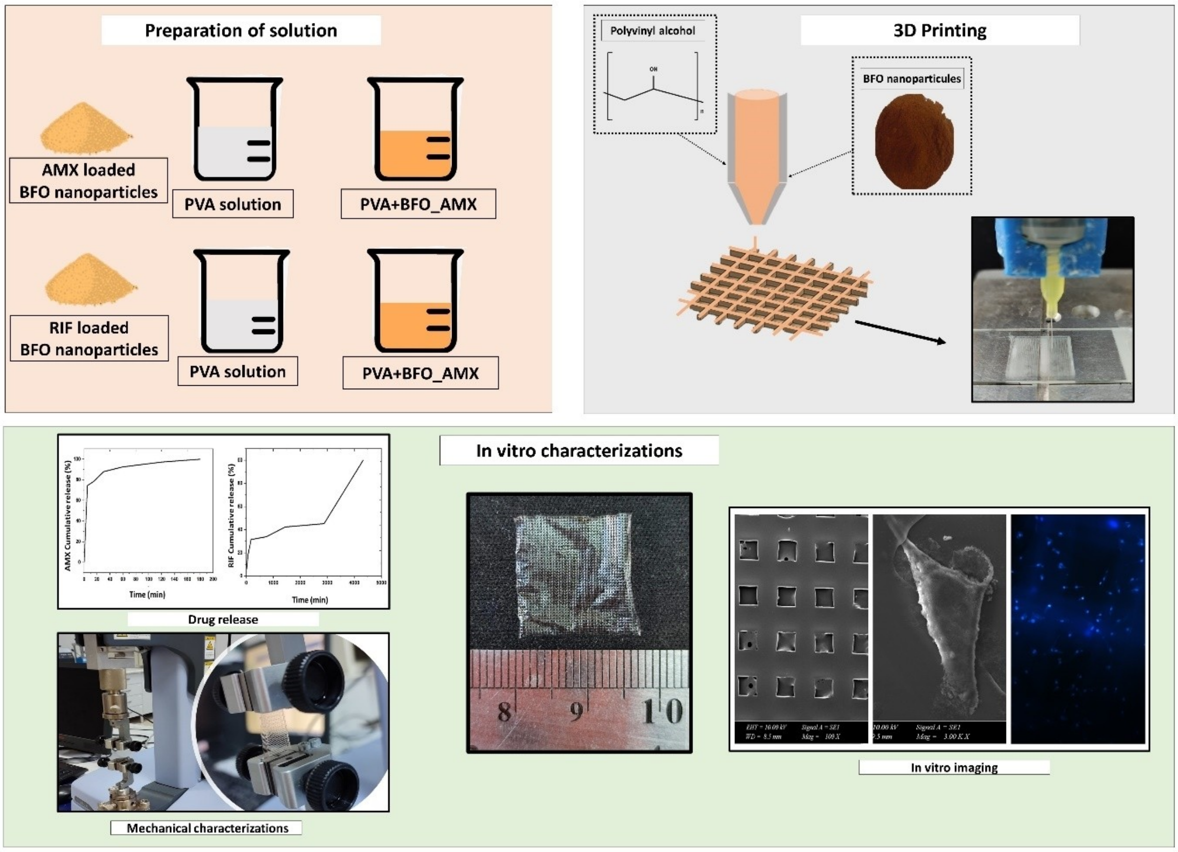

Figure 1. The schematic illustration of the experimental study.

spectroscopy (FTIR, 4700 Jasco, Japan), which has a 4000–400 cm^{-1} scanning range and 4 cm^{-1} resolution.

Morphological Analysis of the Scaffolds

The surface morphology of the 3D scaffolds was analysed using scanning electron microscopy (SEM, EVA MA 10, ZEISS). Before imaging, the surface of the scaffolds was coated with Au for 120 seconds using a coating machine (Quorum SC7620, USA). The Analysis5 (Olympus, USA) software was used to measure the pore sizes.

Thermal Behaviours of the Scaffolds

The thermal properties of the scaffolds were determined using Differential Scanning Calorimetry (DSC, Shimadzu, Japan). The tests were performed at a 25 to 300 °C temperature range at the scanning rate of 10 °C/min.

Mechanical Possessions of the Scaffolds

The mechanical properties of the scaffolds were analysed using a uniaxial tensile tester (Shimadzu, EZ-LX, Japan). Before testing, the thickness values of the scaffolds were measured using a digital micrometre (Mitutoyo MTI Corp., USA). The upper and lower parts of the scaffolds were placed horizontally in the corresponding compartment of the device. 5 mm/min test speed and 5 kN force were applied to all the scaffolds during the test.

Swelling and Degradation of Possessions of the Scaffolds

In the swelling test, scaffolds were placed in 1 mL of phosphate-buffered saline (PBS, pH 7.4). The scaffolds were kept in the thermal shaker (BIOSAN TS-100) at 37 °C for 24 h. The initial weights (W_0) of the scaffolds were measured and recorded. The wet weights (W_w) of the scaffolds were measured every day, and the swelling rate (S_R) was calculated using equation 1.[27]

$$S_R = \frac{W_w - W_0}{W_0}.100 \tag{1}$$

To observe the degradation behaviours of the scaffolds, they were removed from the PBS and put in the oven for 24 h, at 37 °C to dry the scaffolds. Then, all dried scaffolds were weighed and labeled as W_t. The degradation rate (D_R) was calculated using equation 2.[27]

$$D_R = \frac{W_0 - W_t}{W_0}.100 \tag{2}$$

MTT Cytotoxicity Assay, DAPI Staining, and Sem Imaging

Firstly, the scaffolds were sterilised overnight under UV in 96-well plates, and they were incubated with a growth medium (DMEM) which was supplemented with 10% FBS and 0.1 mg/mL penicillin/streptomycin. The incubator had a 37 °C temperature value and a 5% CO_2 atmosphere. The 5×10^4 human adipose tissue-derived mesenchymal stem cells (hAD-MSCs) were seeded onto scaffolds in 96-well plates as in the standard cell culture procedure. The cytotoxicity detection kit (MTT from Glentham Life Sciences) was used to investigate the cytotoxicity properties of the scaffolds after the 1st, 3rd, and 7th days of incubation. The absorbance values were measured with the ELISA reader (Perkin Elmer, Enspire) at a wavelength of 560 nm.

DAPI staining was performed to investigate the attachment of hAD-MSCs to the 3D scaffolds. After 1 and 3 days, the medium was removed, and the scaffolds were rinsed with PBS. After that, all scaffolds were fixed at room temperature for 30 minutes with 4% formaldehyde. Afterwards, the scaffolds were rinsed with PBS and then stained with 1 μg/mL DAPI (Invitrogen), kept at room temperature for 20 minutes to stain the nuclei of the cells. In the final stage, scaffolds were inserted between the slide and coverslip, and the images were taken using an inverted fluorescent microscope (Leica).

SEM imaging was used to examine the cellular morphology of hAD-MSCs on the scaffolds. The growth medium was discarded after 3 days, and all scaffolds were fixed with 4% glutaraldehyde (Sigma), dried with serial ethanol dilutions, and air-dried.

In Vitro Drug Release

The release behaviours of the AMX and RIF from the 13% PVA/BFO_AMX and 13% PVA/BFO_RIF scaffolds were performed with PBS (pH: 7.4) in a thermal shaker (BIOSAN TS-100 C). Firstly, five different (2, 4, 6, 8, and 10 μg/mL) drug concentrations were prepared, and the calibration curves of AMX and RIF were determined in the wavelength range of 190–400 nm. In the release stage, scaffolds were weighed (5 mg) and placed in the eppendorf tubes with 1 mL PBS (pH = 7.4). The absorbance values were taken with a UV spectrophotometer (Shimadzu, Japan). After each measurement, PBS was changed with a fresh one. The absorbance wavelength points were 228 nm and 334 nm for AMX and RIF, respectively.

Results & Discussions

FTIR Analysis

Figure 2 represents the FTIR spectrum of all scaffolds. Figure 2 (a) shows the FTIR spectrum of the BFO particle. The two distinct and strong peaks were observed around 400–550 cm^{-1}. The stretching vibrational modes of Fe–O bonds, which are characteristic of the tetrahedral FeO_4 and octahedral FeO_6 groups in perovskite compounds at 424 cm^{-1} and 524 cm^{-1}.[28] The bands observed between 800 and 1000 cm^{-1} corresponded to the characteristic Fe–O band, confirming the formation of the high crystalline phase, while the bands around 1000 cm^{-1} corresponded to the Bi–O bond's vibrational modes.[29] Figure 2 (b, c) shows the absorption peaks of BFO/AMX and BFO/RIF particles, respectively. The peaks around 1300 cm^{-1} are due to trapped nitrates in the BFO particles.[30] Figure 2 (d) represents the characteristic PVA peaks which are C–H broad alkyl tensile band (2850–3000 cm^{-1}), the strong hydroxyl bands typical for free alcohol (unbonded –OH stretch band at 3600–3650 cm^{-1}), and hydrogen bonded band (3200–3570 cm^{-1}).[31,32] The strong hydroxyl bands, such as the O–H stretch band typical of free alcohol at 3271 cm^{-1}, the C–H alkyl tension band induced in CH_3 bending at 2909 cm^{-1}, and the strong band from the carbonyl group at 1712 cm^{-1} were confirmed.[33] The proportion of crystallinity of PVA can be determined using FTIR spectra. The absorption bands at 1142 and 1712 cm^{-1} are crystallinity-sensitive.[34] Since the PVA is highly hydrolysed, the lack of signal in the 1700 cm^{-1} region indicated that only a small number of acetate groups could be found in the polymer chain.[35] It is caused by coupling OH vibrations at 1371 cm^{-1} and 1425 cm^{-1} with CH wagging vibrations in a 13% PVA scaffold.[36] A strong peak at 1074–1020 cm^{-1} is assigned for a stretching C–O in a C–O–H group.[37] Figure 2 (e, f) showed the absorption peaks of the 13% PVA/(0.075)% BFO_AMX and 13% PVA/(0.075)% BFO_RIF scaffolds, respectively. The O–H stretch band typical for free alcohol at 3271 cm^{-1}, and C–H alkyl tension band peaks induced in CH_3 bending at 2909 cm^{-1} indicated the presence of PVA in the scaffolds. In addition, it showed the presence of trapped nitrates belonging to the 1300 cm^{-1} peak of BFO particles in the scaffolds.

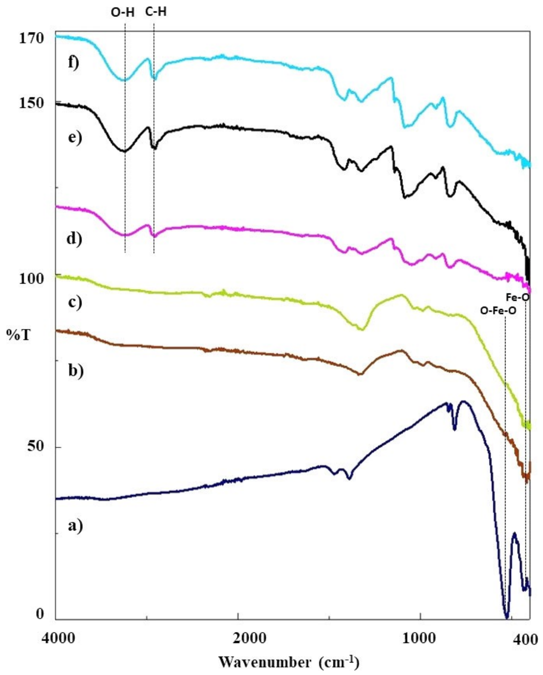

Figure 2. FTIR spectrums of the pure BFO (a), BFO-AMX (b), BFO-RIF (c), 13% PVA (d), 13% PVA/(0.075)% BFO_AMX (e), 13% PVA/(0.075)% BFO_RIF (f).

Morphological Properties of the Scaffolds

The porosity and pore size values are critical for cell proliferation and migration.[38] Figure 3 shows the SEM images and pore size distributions of the scaffolds. Figure 3a represented the 13% PVA scaffold with homogeneous pore size distributions. The mean pore size of the 13% PVA was 211.75 ± 12.82 μm. Figure 3b shows the SEM images and pore size distributions of the 13% PVA/(0.075)% BFO_AMX scaffold, and it had a mean pore size value of 173.25 ± 7.4 μm. In Figure 3c, the pore size of the 13% PVA/(0.075)% BFO_RIF scaffold was 184.08 ± 6.1 μm. The SEM images showed that the AMX and RIF addition decreased the pore size value of the 13%

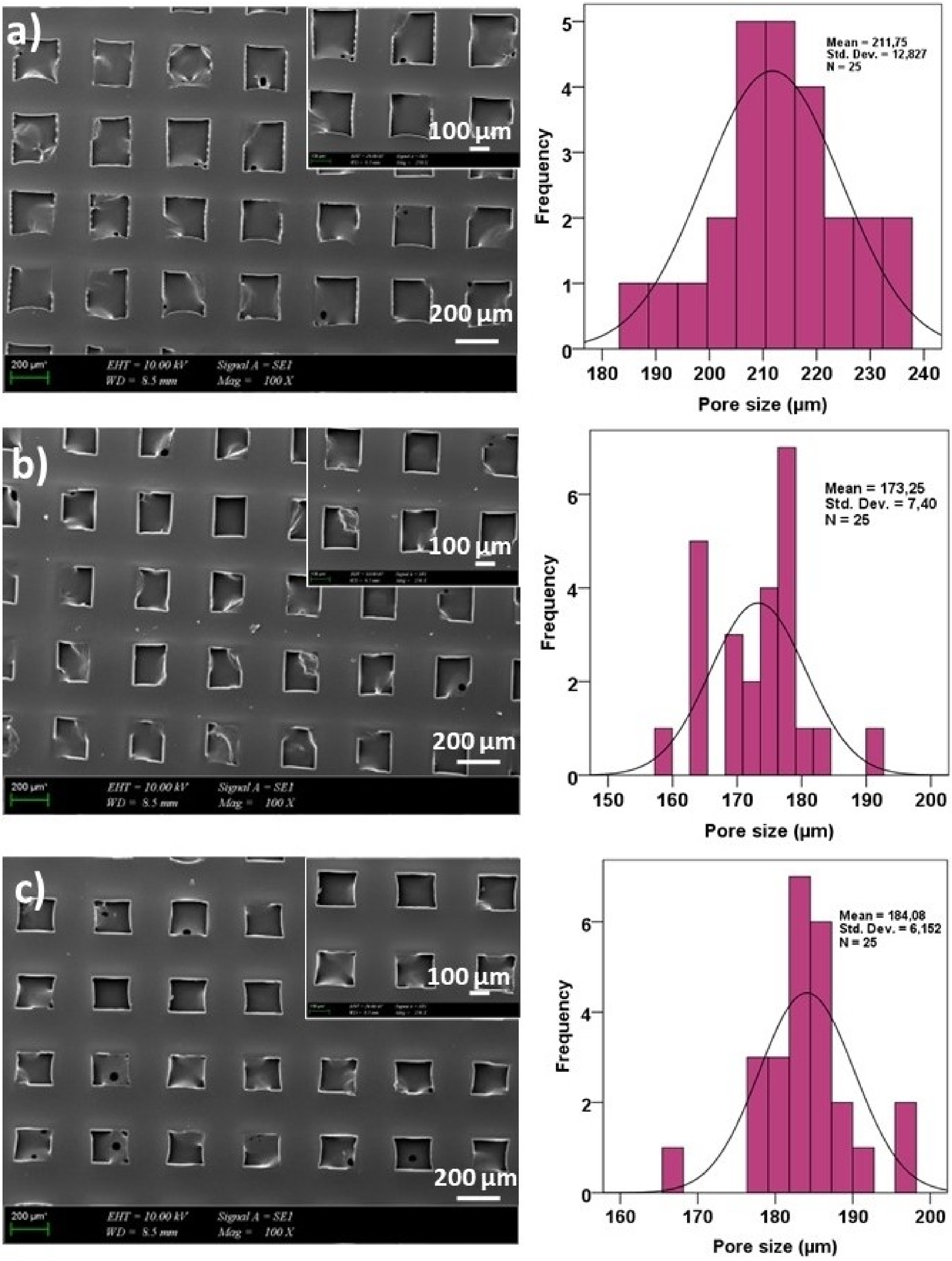

Figure 3. SEM images of the 13 % PVA (a), 13 % PVA/(0.075)% BFO_AMX (b), and 13 % PVA/(0.075)% BFO_RIF (c).

PVA scaffold. The minimum pore size was obtained for 13 % PVA/(0.075)% BFO_AMX scaffold.

DSC Analysis

Figure 4 showed the DSC curves of the synthesized BFO, BFO_AMX, and BFO_RIF particles, 13 % PVA, 13 % PVA/(0.075)% BFO_AMX and 13 % PVA/(0.075)% BFO_RIF scaffolds. The DSC curve of the BFO particles prepared by the co-precipitation method is depicted in Figure 4. The formation of the Bi_2O_3 and Fe_2O_3 phases accounts for

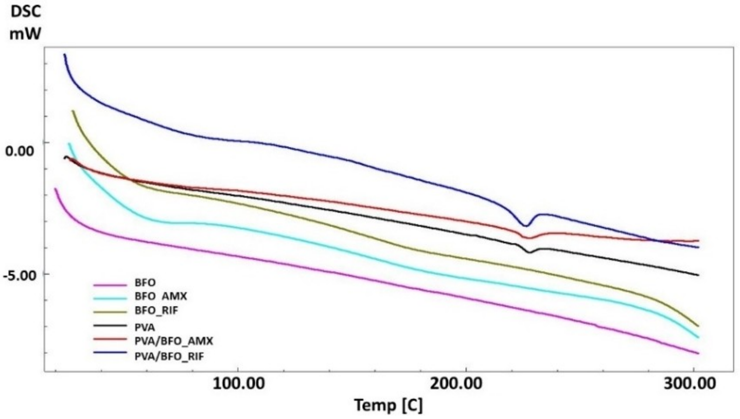

Figure 4. DSC curves of the pure BFO, drugs-loaded BFO, and 3D scaffolds.

the exothermic peak around 285 °C. Furthermore, this peak corresponded to the mass loss caused by the decomposition of $Bi(OH)_3$ and $Fe(OH)_3$.[39] AMX and RIF-loaded BFO particles exhibited similar thermal behaviour to pure BFO particles. The melting point of highly crystalline PVA is approximately 230 °C.[40] In these results, the melting point of the 13 % PVA was found to be 228 °C which is very close to the melting temperature value of pure PVA. In addition, the results showed that the melting temperature of the 13 % PVA did not change significantly with the addition of drug-loaded BFO particles.

Mechanical Properties of the Scaffolds

The structural properties of the scaffolds, such as pore size and porosity, are critical for mechanical qualities and nutrient transport and can potentially alter their performance once they penetrate the defect site.[41] Table 1 showed the tensile test results of the scaffolds. The results indicated that 13 %PVA scaffolds with BFO_RIF particles had the highest tensile strength value (8.92 ± 1.23 MPa) compared to the others. 13 % PVA scaffold had the lowest tensile strength value (6.82 ± 2.61 MPa). 13 % PVA/(0.075)% BFO_AMX and 13 % PVA/(0.075)% BFO_RIF scaffolds exhibited similar tensile properties. According to the results, it can be said that the addition of BFO to the scaffolds caused an increase in strength values. On the other hand, 13 % PVA scaffold had the highest strain at break (62.39 %) value compared to the others. In addition, it was observed that 13 %% PVA/ (0.075)% BFO_RIF scaffolds (45.54 %) had lower strain at break compared to 13 % PVA/(0.075)% BFO_AMX scaffolds (53.24 %). The low interfacial adhesion of PVA and BFO particles is due to poor bonding between PVA and BFO particles.[13] As a result, the addition of BFO to the scaffolds decreased strain at break values since the interaction of PVA and BFO was less.

Table 1. Tensile test results of the scaffolds.

Scaffolds	Tensile strength (MPa)	Strain at break (%)
13 % PVA	6.82 ± 2.61	62.39 ± 4.15
13 % PVA/(0.075)% BFO_AMX	8.40 ± 0.38	53.24 ± 0.35
13 % PVA/(0.075)% BFO_RIF	8.92 ± 1.23	45.54 ± 4.07

Swelling and Degradation Behaviours of the Scaffolds

According to the swelling test results (figure 5A), 13 % PVA (figure 5 (A, a)) showed a high swelling rate since it is a hydrophilic polymer, but the highest swelling rate belonged to the 13 % PVA/(0.075)% BFO_AMX scaffold (figure 5 (A, c)). The swelling rate of 13 % PVA scaffold was lower than 13 % PVA/(0.075)% BFO_RIF (figure 5 (A, b)). The lowest swelling rate on the first day was observed in the 13 % PVA scaffold. After 3 hours of incubation, all scaffolds reached the maximum swelling rate. After this time, swelling rates of all scaffolds started to decrease. When the degradation behaviours of the scaffolds were examined (figure 5B), the lowest degradation rate was observed in the 13 % PVA/(0.075)%BFO_AMX scaffold. It was observed that 13 % PVA and 13 % PVA/(0.075)% BFO_RIF scaffolds showed nearly the same degradation behaviour.

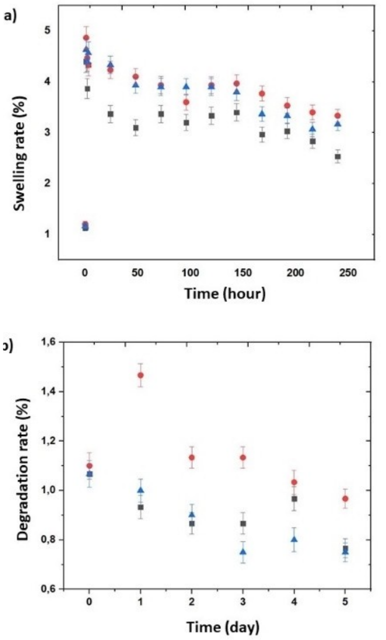

Figure 5. Swelling (A) and degradation (B) graphs of the scaffolds; 13 % PVA (a), 13 % PVA/(0.075)% BFO_RIF (b), and 13 % PVA/(0.075)% BFO_AMX (c).

MTT Assay

The MTT assay was used to assess the biocompatibility of 13 % PVA, 13 % PVA/(0.075)% BFO_AMX, and 13 % PVA/(0.075)% BFO_RIF scaffolds with human adipose tissue-derived mesenchymal stem cells (hAD-MSCs) after 1, 3, and 7 days of incubation. As seen in Figure 6, it was observed that 13 % PVA, 13 % PVA/(0.075)% BFO_AMX, and 13 % PVA/(0.075)% BFO_RIF scaffolds were not cytotoxic compared to the 2D group (control group). After the first day of culture, the results showed that the maximum cell viability (85.8 %) was observed for 13 % PVA/(0.075)% BFO_AMX scaffolds, and minimum cell viability (75.8 %) was detected for 13 % PVA/(0.075)% BFO_RIF scaffolds. The highest cell viability (87 %) was observed in the 13 % PVA scaffold after 3rd day of culture, and the highest viability value (90 %) was observed in the 13 % PVA/(0.075)% BFO_AMX scaffold at the end of the 7th day. In addition, the 13 % PVA and 13 % PVA/(0.075)% BFO_RIF scaffolds had 80 % and 77 % viability values, respectively. According to the results, it can be said that cell growth on the 13 % PVA/(0.075)% BFO_AMX was higher than others.

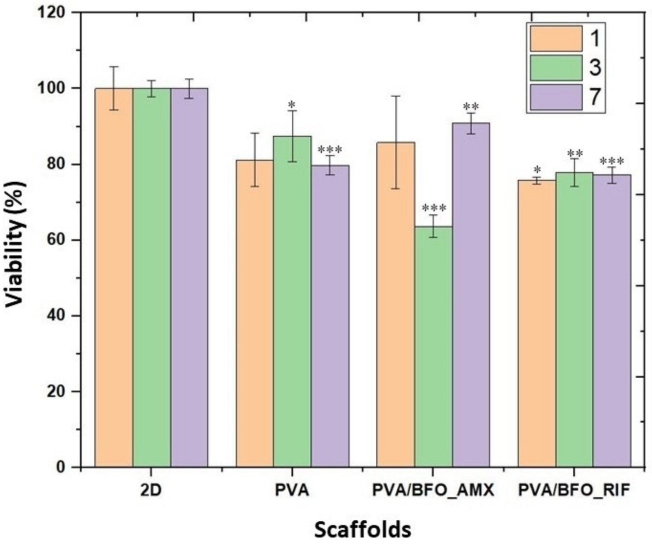

Figure 6. MTT graph of all scaffolds after 1, 3, and 7 days of incubation.

Figure 7 represented the fluorescence images of the DAPI stained hAD-MSCs on 13 % PVA, 13 % PVA/(0.075)% BFO_AMX, and 13 % PVA/(0.075)% BFO_RIF scaffolds after 1st and 3rd days of incubation. According to the images, it can be observed that the cells were more spread on the 13 % PVA/(0.075)% BFO_RIF compared to the 13 % PVA/(0.075)% BFO_AMX scaffold for both 1st and 3rd days of the culture period.

In Figure 8, the cell morphologies on the scaffolds were observed with SEM after 7 days of the culture environment. The human adipose tissue is a good source for collecting human adipose-derived mesenchymal stem cells (hAD-MSCs). They can divide and reproduce themselves repeatedly over a long period.[42] The scaffolds cultured with hAD-MSCs revealed a significant micro-environment for the cells. The cells developed a distinct three-dimensional morphology on the scaffolds, with partial cell-cell interactions.[43] The 13 % PVA/(0.075)% BFO_RIF scaffold showed more significant spreading morphology than the others. According to the results, it can be concluded that strong adhesion and

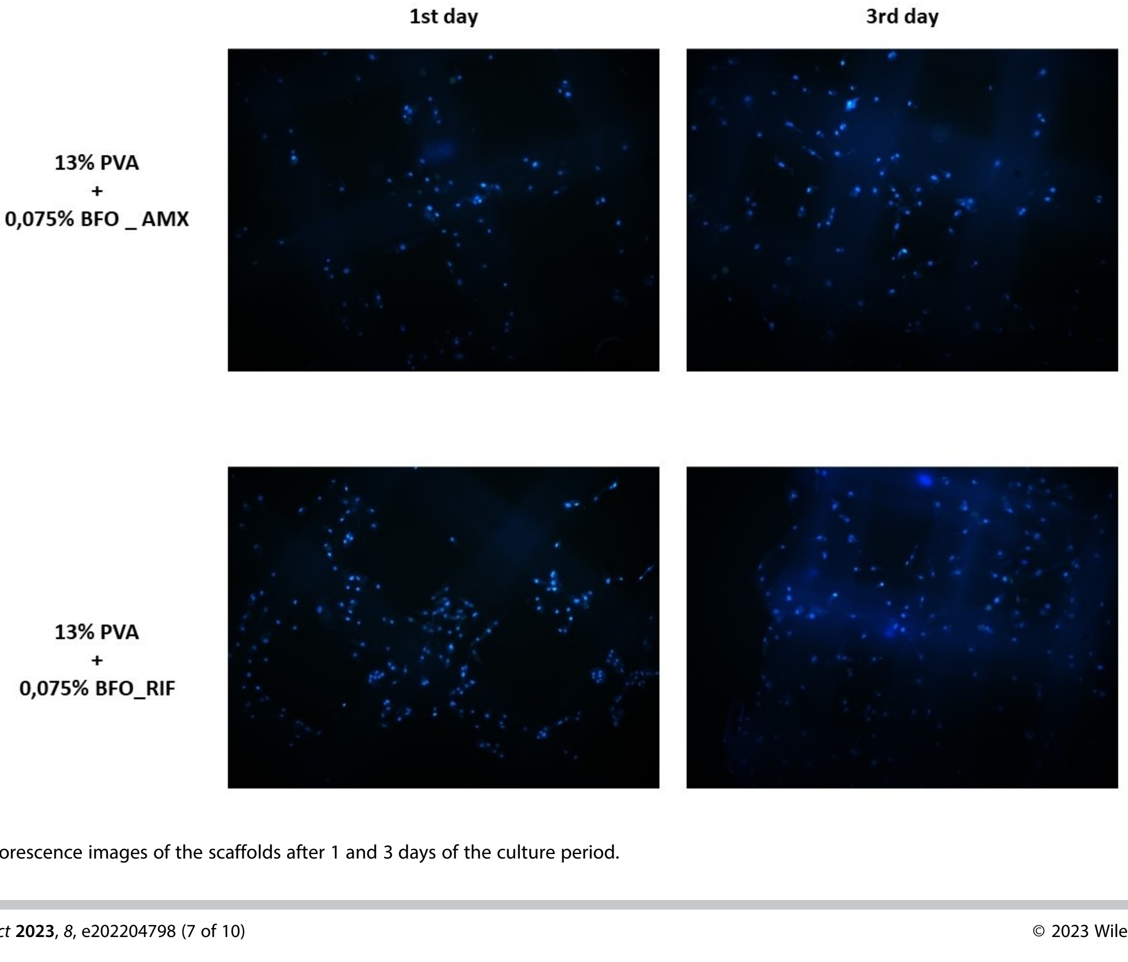

Figure 7. Fluorescence images of the scaffolds after 1 and 3 days of the culture period.

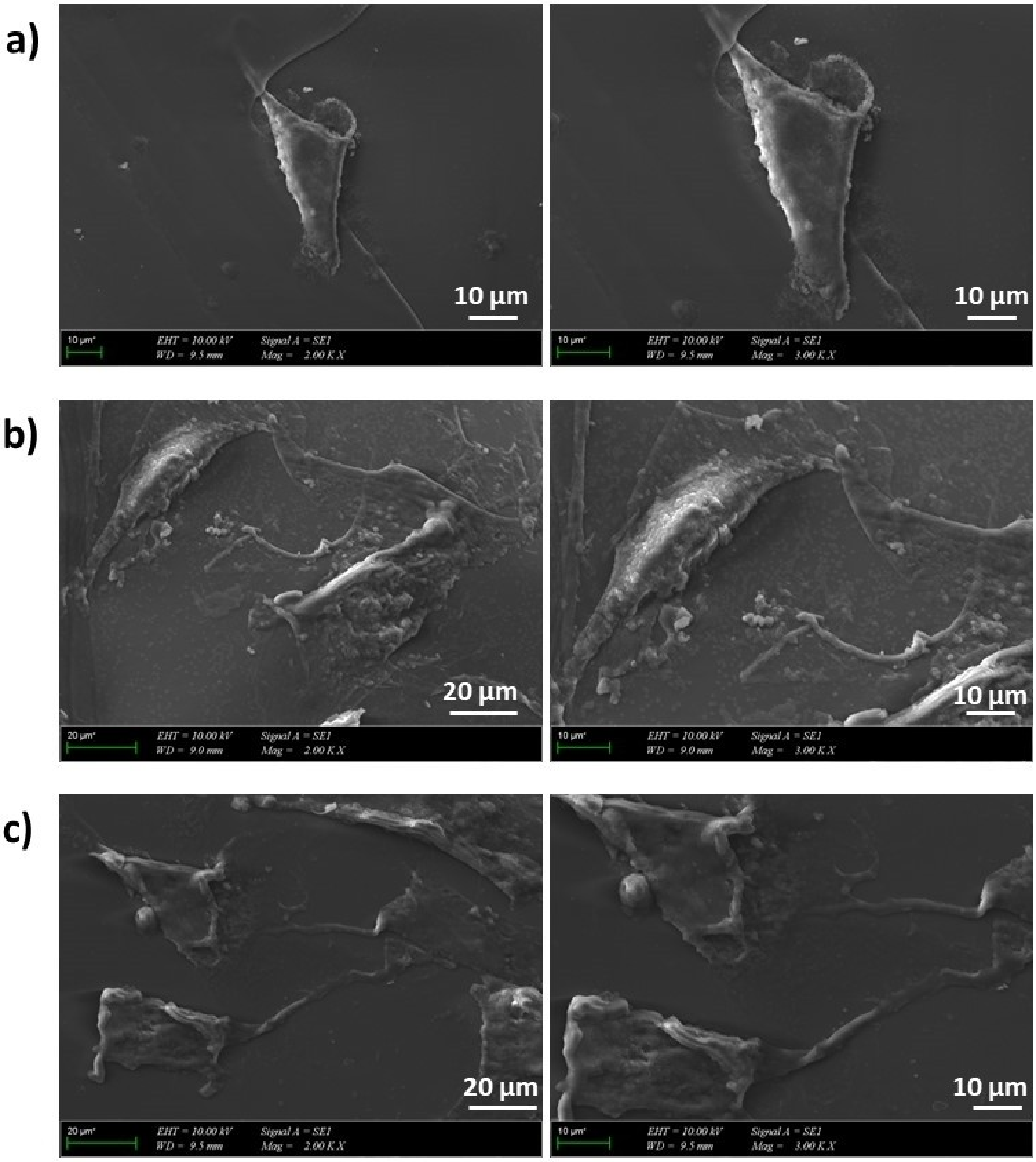

Figure 8. SEM images of the cells on the scaffolds after 7 days of incubation, 13 % PVA (a), 13 % PVA/(0.075)% BFO_AMX (b), and 13 % PVA/(0.075)% BFO_RIF (c).

proliferation were observed, proving the biocompatibility of all scaffolds.

AMX and RIF Release from the 13 % PVA/(0.075)% BFO Scaffolds

The AMX has a short (1–1.5 hours) circulating half-life after oral administration, necessitating frequent dosing to keep blood plasma concentrations steady. Therefore, achieving controlled or continuous drug delivery is crucial to boost stability or bioavailability and direct the drug delivery to a specific site.[44] The release of AMX from scaffolds was examined in a thermal shaker at pH 7.4. The calibration curve of AMX was obtained from stock solutions (0.2, 0.4, 0.6, 0.8 and 1.0 µg/mL) and is given in Figure 9a. Figure 9b represents the absorbance plot of the AMX at 228 nm. Figure 9c shows the cumulative release behaviour of the AMX from the 13 % PVA/(0.075)% BFO scaffold. The results showed that during the 15 minutes, 79 % of the AMX was released from the scaffolds, which is attributed to the quite water-soluble properties of PVA. After 30 minutes, 88 % of cumulative release was obtained, and the whole AMX (100 %) was released from the scaffolds after 180 minutes.

Figure 9d shows the calibration curve of the RIF. In this figure, five different ratios of stock solutions (0.2, 0.4, 0.6, 0.8 and 1.0 µg/mL) were prepared and absorbance values were obtained at 334 nm (figure 9e). Figure 9f represents the cumulative release behaviour of the RIF from the 13 % PVA/(0.075)% BFO scaffolds. The 7 % of

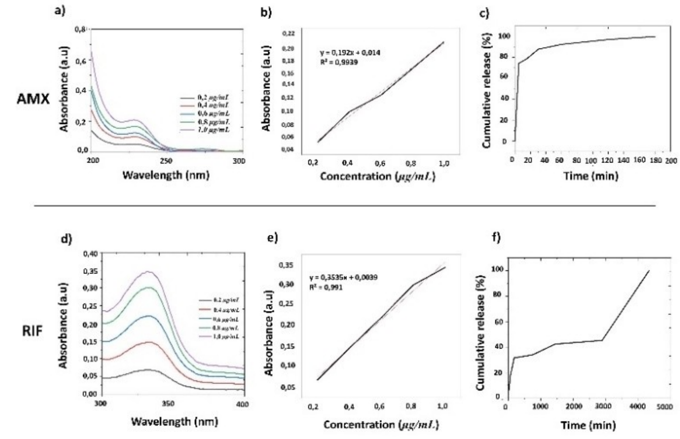

Figure 9. The calibration curve of AMX (a), absorbance graph obtained at 228 nm (b), and cumulative release behaviour of the AMX from the scaffolds (c), the calibration curve of RIF (d), absorbance graph obtained at 334 nm (e), and cumulative release behaviour of the RIF from the scaffolds (f).

cumulative release was obtained in the first 15 minutes. The release amount reached 32% after 300 minutes. After 3 days, 100% of RIF was released from the scaffold.

Conclusions

In this study, drug-loaded bismuth ferrite-doped PVA scaffolds were successfully produced using a 3D printer. The homogeneous pore structures were observed for all scaffolds according to the SEM images. The pore size ranged from 170 to 210 μm. It is observed that the pore size value did not significantly alter by the addition of AMX and RIF-loaded BFO. DSC results showed that drug-loaded BFO particles did not change the specific thermal points of the PVA scaffolds significantly. As a result of FTIR analysis, characteristic peaks of 13% PVA and drug-loaded BFO were observed in the scaffolds and the addition of drug-loaded BFO in the 13% PVA solution did not cause significant shift in the main peaks of 13% PVA. According to the release test, it was observed that the AMX-loaded BFO particles were rapidly released from the scaffolds and the RIF-loaded BFO particles demonstrated a more controlled release. According to the biocompatibility test results, it can be concluded that both AMX and RIF-loaded 13% PVA/(0.075)% scaffolds are biocompatible and can be used in wound dressing applications. This study also showed that BFO has the potential to be used for electrically controlled drug release applications as a further studies.

Conflict of Interests

The authors declare no conflict of interest.

Data Availability Statement

The data that support the findings of this study are available from the corresponding author upon reasonable request.

Keywords: Bismuth ferrite · controlled drug delivery · polyvinyl alcohol · 3D printing · wound dressing

[1] R. Laurano, M. Boffito, M. Abrami, M. Grassi, A. Zoso, V. Chiono, G. Ciardelli, *Bioact. Mater.* **2021**, *6*, 3013.
[2] A.-M. Croitoru, Y. Karaçelebi, E. Saatcioglu, E. Altan, S. Ulag, H. K. Aydoğan, A. Sahin, L. Motelica, O. Oprea, B.-M. Tihauan, R.-C. Popescu, D. Savu, R. Trusca, D. Ficai, O. Gunduz, A. Ficai, *Pharmaceutica* **2021**, *13*, 957.
[3] R. G. Frykberg, J. Banks, *Adv. Wound Care* **2015**, *4*, 560.
[4] S. Dhivya, V. V. Padma, E. Santhini, *Biomedicine* **2015**, *5*, 22.
[5] P. Kaiser, J. Wächter, M. Windbergs, *Drug Delivery Transl. Res.* **2021**, *11*, 1545.
[6] F. Tsegay, M. Elsherif, H. Butt, *Polymer* **2022**, *14*, 1012.
[7] T. Maver, D. M. Smrke, M. Kurečič, L. Gradišnik, U. Maver, K. Stana Kleinschek, *J. Sol-Gel Sci. Technol.* **2018**, *88*, 33.
[8] M. E. Mutlu, S. Ulag, M. Sengor, S. Daglılar, R. Narayan, O. Gunduz, *Mater. Lett.* **2021**, *305*, 130844.
[9] S. Saghazadeh, C. Rinoldi, M. Schot, S. S. Kashaf, F. Sharifi, E. Jalilian, K. Nuutila, G. Giatsidis, P. Mostafalu, H. Derakhshandeh, K. Yue, W. Swieszkowski, A. Memic, A. Tamayol, A. Khademhosseini, *Adv. Drug Delivery Rev.* **2018**, *127*, 138.
[10] D.-E. Lee, H. Koo, I.-C. Sun, J. H. Ryu, K. Kim, I. C. Kwon, *Chem. Soc. Rev.* **2012**, *41*, 2656.
[11] L. Zhang, D. Pornpattananangku, C.-M. J. Hu, C.-M. Huang, *Curr. Med. Chem.* **2010**, *17*, 585.
[12] H. Koo, M. S. Huh, I.-C. Sun, S. H. Yuk, K. Choi, K. Kim, I. C. Kwon, *Acc. Chem. Res.* **2011**, *44*, 1018.
[13] T. Bedir, S. Ulag, K. Aydogan, A. Sahin, B. Karademir Yilmaz, Y. Guvenc, M. Bozlar, C. B. Ustundag, O. Gunduz, *Polym. Adv. Technol.* **2021**, *32*, 1114.
[14] A. K. Pradhan, K. Zhang, D. Hunter, J. B. Dadson, G. B. Loiutts, P. Bhattacharya, R. Katiyar, J. Zhang, D. J. Sellmyer, U. N. Roy, Y. Cui, A. Burger, *J. Appl. Phys.* **2005**, *97*, 093903.
[15] S. Ulag, C. Kalkandelen, T. Bedir, G. Erdemir, S. E. Kuruca, F. Dumludag, C. B. Ustundag, E. Rayaman, N. Ekren, B. Kilic, O. Gunduz, *Mater. Sci. Eng. B* **2020**, *261*, 114660.
[16] Z. Liu, Y. Qi, C. Lu, *J. Mater. Sci. Mater. Electron.* **2009**, *21*, 380.
[17] X. Bai, J. Wei, B. Tian, Y. Liu, T. Reiss, N. Guiblin, P. Gemeiner, B. Dkhil, I. C. Infante, *J. Phys. Chem. C* **2016**, *120*, 3595.
[18] S. Jiang, S. Liu, W. Feng, *J Mech. Behav. Biomed. Mater.* **2011**, *4*, 1228.
[19] F. Martínez-Gómez, J. Guerrero, B. Matsuhiro, J. Pavez, *Carbohydr. Polym.* **2017**, *155*, 182.
[20] S. Ulag, E. Ilhan, R. Demirhan, A. Sahin, B. K. Yilmaz, B. Aksu, M. Sengor, D. Ficai, A. M. Titu, A. Ficai, O. Gunduz, *Molecules* **2021**, *26*, 2577.
[21] Q. Luo, Y. Shan, X. Zuo, J. Liu, *RSC Adv.* **2018**, *8*, 13284.
[22] G. Rivera-Hernández, M. Antunes-Ricardo, P. Martínez-Morales, M. L. Sánchez, *Int. J. Pharm.* **2021**, *600*, 120478.
[23] C. Kalkandelen, S. Ulag, B. Ozbek, G. O. Eroglu, D. Ozerkan, S. E. Kuruca, F. N. Oktar, M. Sengor, O. Gunduz, *ChemistrySelect* **2019**, *4*, 12032.
[24] G.-M. Lemnaru (Popa), R. D. Truşcă, C.-I. Ilie, R. E. Tiplea, D. Ficai, O. Oprea, A. Stoica-Guzun, A. Ficai, L.-M. Diţu, *Molecules* **2020**, *25*, 4069.
[25] K. Irem Deniz, S. Ulag, O. Gunduz, *Mater. Lett.* **2022**, *324*, 132664.
[26] N. V. Chokshi, H. N. Khatri, M. M. Patel, *Drug Dev. Ind. Pharm.* **2018**, *44*, 1975.
[27] E. de Souza Costa-Júnior, M. M. Pereira, H. S. Mansur, *J. Mater. Sci. Mater. Med.* **2009**, *20*, 553.
[28] C. Chen, J. Cheng, S. Yu, L. Che, Z. Meng, *J. Cryst. Growth* **2006**, *291*, 135.
[29] I. O. Troyanchuk, A. N. Chobot, O. S. Mantytskaya, N. V. Tereshko, *Inorg. Mater.* **2010**, *46*, 424.
[30] M. Muneeswaran, P. Jegatheesan, N. V. Giridharan, *J. Exp. Nanosci.* **2013**, *8*, 341.
[31] S. Ulag, E. Ilhan, A. Sahin, B. Karademir Yilmaz, D. M. kalaskar, N. Ekren, O. Kilic, F. Nuzhet Oktar, O. Gunduz, *Eur. Polym. J.* **2020**, *133*, 109744.
[32] H. S. Mansur, R. L. Oréfice, A. A. P. Mansur, *Polymer* **2004**, *45*, 7193.
[33] H. S. Mansur, C. M. Sadahira, A. N. Souza, A. A. P. Mansur, *Mater. Sci. Eng. C* **2008**, *28*, 539.
[34] N. V. Bhat, M. M. Nate, M. B. Kurup, V. A. Bambole, S. Sabharwal, *Nucl. Instrum. Methods Phys. Res. Sect. B* **2005**, *237*, 585.

[35] A. Bernal-Ballen, J. Lopez-Garcia, M.-A. Merchan-Merchan, M. Lehocky, *Molecules* **2018**, *23*, 3109.

[36] P. K. Khanna, N. Singh, S. Charan, V. V. V. S. Subbarao, R. Gokhale, U. P. Mulik, *Mater. Chem. Phys.* **2005**, *93*, 117.

[37] N. V. Petrova, A. M. Evtushenko, I. P. Chikhacheva, V. P. Zubov, I. V. Kubrakova, *Russ. J. Appl. Chem.* **2005**, *78*, 1158.

[38] S. J. Hollister, *Nat. Mater.* **2005**, *4*, 518.

[39] M. Sakar, S. Balakumar, P. Saravanan, S. N. Jaisankar, *Mater. Res. Bull.* **2013**, *48*, 2878.

[40] A. Sionkowska, A. Płanecka, J. Kozłowska, J. Skopińska-Wiśniewska, *CL* **2010**, *1*, 112.

[41] R. Stangl, B. Rinne, S. Kastl, C. Hendrich, R. Stangl, *Eur. Cells Mater.* **2001**, *2*, 1–9.

[42] S.-D. Lin, K.-H. Wang, A.-P. Kao, *Tissue Eng. A* **2008**, *14*, 571.

[43] S.-J. Heo, S. E. Szczesny, D. H. Kim, K. S. Saleh, R. L. Mauck, *J. Orthop. Res.* **2018**, *36*, 808.

[44] E. Güncüm, N. Işıklan, C. Anlaş, N. Ünal, E. Bulut, T. Bakırel, *Artif. Cells, Nanomed., Biotechnol.* **2018**, *46*, 964.

Submitted: December 13, 2022
Accepted: April 24, 2023